Microstructure and mechanical properties of in-situ SiO$_2$-reinforced mechanically alloyed CoCrFeNiMnX (X= 5, 20, 35 at.%) high-entropy alloys

Filip Průša [a,*], Petr Kratochvíl [a], Angelina Strakošová [a], Miroslav Karlík [b,d], Andrea Školáková [a], Jaroslav Čech [b], Petr Haušild [b], Jiří Čapek [b], Marek Vronka [c], Jozef Veselý [d], Hana Thürlová [a], Marcello Cabibbo [e], Ondřej Jankovský [f]

[a] University of Chemistry and Technology, Prague, Department of Metals and Corrosion Engineering, Technicka 5, 166 28, Prague 6, Czechia
[b] Czech Technical University in Prague, Faculty of Nuclear Sciences and Physical Engineering, Trojanova 13, 120 00, Prague 2, Czechia
[c] Institute of Physics of the Czech Academy of Sciences, Na Slovance 1999/2, 182 21, Prague 8, Czechia
[d] Charles University, Faculty of Mathematics and Physics, Ke Karlovu 5, 121 16, Prague 2, Czechia
[e] DIISM / Universita Politecnica Delle Marche, Via Brecce Bianche 12, I-60131, Ancona, Italy
[f] University of Chemistry and Technology, Prague, Department of Inorganic Chemistry, Technicka 5, 166 28, Prague 6, Czechia

ARTICLE INFO

ABSTRACT

The CoCrFeNiMnX (X = 5, 20, and 35 at.%) alloys, reinforced with 5 at.% SiC powder, were prepared by mechanical alloying and spark plasma sintering. This preparation method resulted in microstructural refinement of the FCC solid solution grains, while the SiC addition reacted with residual oxygen to form homogeneously distributed ultrafine SiO2 particles. Additionally, the alloys contained Cr7C3 carbides, which were significantly larger than the SiO2 particles and enriched with the alloy's elements, including Mn. Among the tested materials, the reinforced CoCrFeNiMn20 alloy exhibited the highest hardness and compressive yield strength (CYS), achieving 392 ± 9 HV30 or 476 ± 3 HVIT1 and 1024 ± 18 MPa, respectively. This alloy also maintained superior CYS (956 ± 35 MPa) even after 100 h of annealing at 800 °C. The reduction in CYS after annealing was smallest for the CoCrFeNiMn5 alloy (35 MPa) and increased with higher Mn content, highlighting Mn's significant role in diffusion-related processes. At elevated temperatures (600 and 800 °C), the CoCrFeNiMn5 alloy had the highest CYS of 190 ± 33 MPa, while the CoCrFeNiMn35 alloy had the lowest at 80 ± 6 MPa. This trend was also observed in wear rate tests, where the CoCrFeNiMn5 alloy had the lowest specific wear rate coefficient of 3.54 ± 0.09 × 10-4 mm^3 N^{-1} m^{-1}. This was due to matrix softening and oxide lubrication without significant spalling. Thus, the CoCrFeNiMn5 alloy demonstrated superior mechanical properties and wear resistance under various conditions, making it a promising candidate for applications requiring high strength and durability.

1. Introduction

High-entropy alloys (HEAs) were firstly reported in 2004 [1] and since then the attention has been exponentially increasing every year. Newly announced results show their superiority compared to conventional alloys. The variety of possible compositions combining 4 or more elements with concentrations ranging between 5 and 35 at. % [2–4] opens many promising research directions. The CoCrFeNiMn alloy belongs to the most studied materials that offer a decent combination of

mechanical properties while mostly retaining a single-phase nature [5–7].

As in the case of other materials, the resulting phase composition and microstructure appearance of the HEAs are affected by the preparation route. The as-cast CoCrFeNiMn alloys show the presence of a single-phase face-centred cubic (FCC) solid solution with dendritic morphology, capable to dissolve also other elements like Nb, Ti, and V [6]. To refine the microstructure, the alloy is commonly processed by intensive plastic deformation methods like rotary swaging [8], cold

---

drawing [9], cold rolling [10–12], cold shape rolling [13], high-pressure torsion (HPT) [14] or equal channel angular pressing (ECAP) [15] and is typically accompanied by a thermal treatment [8,16] allowing partial recrystallization and precipitation of newly formed phases within the microstructure. Powder metallurgy (PM) techniques are known as effective methods for significant refinement of the microstructure without subsequent thermal treatment. More importantly, mechanical alloying is one of the PM techniques that can be considered a non-equilibrium process that often results in phase transformations during hot compaction [17,18].

During long-term annealing at temperatures between 500 and 700 °C, new phases, that were enriched with various elements, are likely to precipitate from CoCrFeNiMn alloy FCC solid solution [19–22]. However, these phases do not form when the annealing temperature reaches 900 °C and the microstructure remains single-phased [21]. The CoCrFeNiMn alloy is well known for its interesting mechanical properties showing high fracture toughness reaching up to 200 MPa m$^{1/2}$ [23, 24]. A key aspect refers to the alloy mechanical properties that are increasing by cooling down to 77 K [5,24]. Further improvement of mechanical properties can be achieved by different methods of refining the microstructure down to an ultrafine-grained scale while allowing deliberate precipitation of new phases within the microstructure [10,15, 25]. Shahmir et al. [15] reported an increase in the ultimate tensile strength (UTS) up to 1080 MPa while maintaining 30 % elongation to failure. The relatively high UTS of the CoCrFeNiMn alloy was further increased by Schuh et al. [25] using an HPT technique reaching a UTS of 1950 MPa and hardness of 520 HV. However, such results were achieved at the expense of ductility loss.

The phase composition and thus the mechanical properties are closely related to the content of each element within the alloy. Therefore, the influence of Ni and Co content was studied in the work of Zhu et al. [26] who investigated (CoCrFeMn)$_{100-x}$Ni$_x$ (x = 0, 5, 10, 12.5, 15, 20, 27.3, 33.3, 42.9) and (CrFeMnNi)$_{100-x}$Co$_x$ (x = 0, 5, 10, 15, 20, 33.3) alloys. In the case of the former alloy, the increasing content of Ni exceeds 15 at. % favoured the stabilization of the FCC solid solution instead of the formation of a mixture of FCC and tetragonal σ phase that was found to coexist while the content of Ni was lower. Similar behaviour was also observed in the case of the latter alloy, where the FCC solid solution and σ phase coexisted within the concentration of Co below 5 at. %. This illustrates that even though the CoCrFeNiMn alloy belongs to one of the most studied alloys, information about the influence of the content of alloying elements is lacking. Accordingly to this, in the recent work of Thurlova et al. [27], the senary alloy substituting the Mn by Al in the CoCrFeNiMn XAl20-x shows another highly perspective approach to increasing the overall performance of the CoCrFeNiMn alloys. Complete substitution of Mn in the CoCrFeNiMn alloy by Al and the influence of its content is then described in the work of Strakosova et al. [28], reporting an increase of the hardness reaching its maxima of 732 HV 30 in the CoCrFeNiAl30 alloy. Replacing the Al in the equiatomic CoCrFeNiAl for Ti increases the hardness even beyond this value, reaching 757 HV 30, as reported in the work of Kratochvil et al. [29]. As demonstrated, substituting Mn with other elements substantially alters the phase compositions, leading to diverse mechanical properties and behaviors. However, a study on the influence of Mn content in short-term mechanically alloyed CoCrFeNiMn alloys has not yet been published. Generally, Mn content affects not only the strength of CoCrFeNi-based alloys through solid solution strengthening nut also the ductility enhancing the damage tolerances, as previously noted by other researchers [30–33].

Except for the aforementioned approaches used for improving the properties of HEAs, oxide dispersion strengthening [34] or carbide particle strengthening [35,36] are currently of interest since they may have a more significant impact on the properties of such alloys that are further retained even at elevated temperatures. Considering the strengthening effect, the matrix material shall be chosen in respect of being able to positively outbalance the brittleness that might arise from

reinforcing with such strengthening particles. From this point of view, it seems a highly viable approach for fine-tuning the properties of ductile HEAs, such as CoCrFeNiMn, by adding a small amount of either oxide or carbide-based particles towards the prepared alloy. Not only the character of the particles, as well as their chemical compositions, amount, and, foremostly their incorporation strategy, are having the most significant influence on the resulting properties. Therefore, homogeneous dispersion of reinforcing particles, often achieved via a combination of mechanical alloying, not only significantly refines the microstructure but also enhances the mechanical properties.

The present manuscript reports the influence of Mn content on the properties of mechanically alloyed CoCrFeNiMnX (X = 5, 20, 35 at. %) alloy reinforced with SiC particles and compacted via spark plasma sintering. As there are still only occasional publications focused on mechanically alloyed HEAs, the present research tends to widely describe one of the most typical HEAs reinforced with one of the lowest amounts of particles in spite of retaining the ductility of the alloys. This approach, combining the intended reinforcement via SiC addition into various Mn-content CoCrFeNi alloys, was chosen for further increasing the mechanical properties of such prepared alloys, respecting the varying content of Mn. It was found, that the reinforcing SiC underwent an in-situ reaction, forming a SiO$_2$ compound, while an unexpected Cr$_7$C$_3$ reinforcing phase formed within the alloy, affecting the overall alloys properties.

2. Materials and methods

The CoCrFeNiMnX (X = 5, 20, 35 at.%) alloy (further denoted also as Mn5, Mn20, and Mn35) has been prepared by mixing the pure elements of Co (2 µm, 99.8%), Cr (44 µm, ≥99%), Fe (5–9 µm, 99.9%), Ni (10 µm, 99.5%), and Mn (≤10 µm, 99.6 %) in suitable ratios forming a 20 g powder batch. Furthermore, 5 at. % of SiC (≤74 µm, ≥97.5%) was added to each of these mixtures to create reinforced composite-like alloys. This mixture was then placed in an AISI 420 stainless steel jar together with milling balls (weight ratio of ≈1:15) and 4 wt % of n-heptane acting as process control agent (PCA) sufficiently decreasing the excessive cold welding. The mechanical alloying (MA) was performed using a Retsch PM 100 milling device operated at 400 rpm in 30 min alloying segments followed by 10 min cool-off pauses to obtain a total alloying time of 8 h. The MA powders were then compacted using a spark plasma sintering device FCT Systeme HP-D 10. For this purpose, 10 g of the powder was closed in a graphite mould and compacted using a heating rate of 200 °C min^{-1} until the compaction temperature of 1000 °C, previously optimized in the work [37], was reached. After this, the powder was compacted at a pressure of 48 MPa and remained compressed at the temperature for 10 min. As a result, a round sample with a 20 mm diameter and ≈4 mm height was obtained and used for further investigations. The phase composition of the powders and compacts and the overall chemical composition of compact samples were determined using X-ray diffraction (XRD) (PANalytical X'Pert Pro, MPD, CoKα$_1$, λ = 1.78901 x10^{-10} m) and X-ray fluorescence (XRF) analysis (ARL XP 2400), respectively. The measured diffraction patterns and phase weight percentages were evaluated with the X'Pert HighScorePlus program using the Rietveld refinement method, based on the minimalization of the difference between measured and computed/refined data; the crystalline phases were identified using the PDF-2 database. Prepared compact samples were cut into different pieces to observe the microstructure and to determine the mechanical properties using Leco VariCut precise laboratory saw equipped with a diamond cutting blade. Standard metallographic cross-sections were examined using an Olympus PME-3 light microscope. The surface porosity was determined before etching, which was afterwards done using diluted aqua regia (mixture of HNO$_3$ and HCl in the ratio of 1:3, further diluted 1:1 with distilled H$_2$O). Porosity and area fractions of oxides/carbides on light microscopy (LM) or scanning (transmission) electron microscopy S(T)EM micrographs were evaluated using the threshold method in the ImageJ software. A

more detailed analysis of the microstructure was carried out using scanning electron microscopy (SEM, JEOL JSM IT500HR, 10 kV), and scanning-transmission electron microscopy (STEM, JEOL JEM-2200FS, 200 kV) equipped with energy dispersion spectrometer (EDS, JEOL Centurio) and NanoMEGAS precession diffraction unit. The lamellae for STEM were prepared by a Ga$^+$ focused ion beam (FIB, FEI Quanta DualBeam).

The mechanical properties were determined by at least 10 individual measurements of the Vickers hardness on each alloy using a load of 30 kg and a dwell time of 10 s. The instrumented (IT – loading-unloading) Vickers microhardness and Young's modulus measurements were using a 1 kg load (MHT, Anton Paar Tritec). At least 10 individual measurements as in the case of the previously mentioned Vickers hardness measurements. This allowed to determine the confidence intervals for each measurements using a level of significance α = 0.05. The compressive stress-strain tests were performed with the universal testing device LaborTech 5.250SP, where the deformation of the miniaturized sample was determined by the upper crosshead movement. For this purpose, miniaturized quadrangular prismatic samples with a height of 1.5 × the size of the base were cut and ground on a P800 abrasive paper. The tests were carried out testing at least 3 samples with a strain rate of 10^{-3} s^{-1} for each of the chosen conditions comprised of testing at the laboratory temperature in the as-compacted state and after 100h annealing at 800 °C, also at elevated temperatures of 600 °C and 800 °C. The values of either the Vickers hardness measurements or the compressive yield strengths (CYS) are accompanied by calculated 95% confidence intervals.

The tribological properties of the samples were also investigated using a linear sliding setup (TRIBOtechnic, Clichy, France). The tests were performed on the ground and polished samples whose surface roughness was measured by a profilometer before the test to assure almost identical starting conditions. An Al$_2$O$_3$ ball (6 mm in diameter, loaded with 5 N) was moving at a speed of 10 mm s^{-1} across the sample surface until reaching a total sliding length of 15 m. The temperature and humidity during the whole test were monitored as being almost constant (23.5 °C and 31.5%). The track profile was measured with the profilometer at three different positions to determine the average cross-sectional area used for the software in-build calculation of the specific wear rate coefficient W_s accordingly to Eq. (1):

$$W_S = \frac{S_{cross} \bullet E}{L \bullet D} \tag{1}$$

where S_{cross} is the cross-sectional area (mm^2), E is the excenter length (mm), L is the normal load (N), and D is the total sliding distance (m). Furthermore, the wear track was investigated using SEM (TESCAN LYRA, 15 kV, BSE + SE mixed 80/20) equipped with an energy dispersion spectrometer (EDS, Oxford, 80 mm^2) to determine the mechanism of wear.

3. Results and discussion

3.1. Chemical and phase composition

To maintain the maximal homogeneity of the powder mixture, similar-sized powders of high-purity elements, were used for the mechanical alloying. As is shown in Table 1, the chemical composition of

Table 1
Chemical composition of the investigated MA + SPS alloys determined by XRF (in at.%).

Sample	Chemical composition [at.%]					
	Co	Cr	Fe	Ni	Mn	Si
CoCrFeNiMn5	22.2	21.7	26.1	22.8	5.1	2.1
CoCrFeNiMn20	17.5	18.4	25.5	19.4	16.8	2.3
CoCrFeNiMn35	16.2	15.0	20.5	16.4	29.5	2.4

the investigated alloys somewhat differs from desired values in favour of a slightly larger Fe content. This is due to the formation of solid solutions leading to a sharp hardness rise that intensified the wear of the alloying jar and favoured Fe content in the alloy. Therefore, it is difficult to preserve a precise composition during MA, as it changes over time. On the other hand, the rest of the elements forming the alloys, except for varied Mn concentration, showed fairly equal/or targeted content. Similar behaviour was also reported by Wu et al. [38], who associated the lower content of Mn within the arc-melted CoCrFe-based alloys with peroxidation of the powders as well to the high partial pressure of its fumes.

Apart from that, all the alloys were containing Si whose content ranged from 2.1 up to 2.4 at.%, corresponding to the addition of 5 at. % of SiC. Furthermore, as it was discovered, the SiC transformed into SiO$_2$ particles during the MA process, which content, considering the above-mentioned amount of SiC, was calculated as 1.84 wt% (for Mn5 alloy) and 1.85 wt% (for Mn20 and Mn35 alloys). The amount of other contaminants did not exceed 0.1 at.% in each of the MA + SPS alloys.

Fig. 1 shows X-ray diffraction patterns of the MA + SPS alloys. The existing phases were identified as FCC solid solution matching the reference card of γ-Fe (JCPDS card no. 33–397, space group Fm3m) and as Cr$_7$C$_3$ chromium carbide (JCPDS card no. 36–1482, space group Pmcn). As follows from Fig. 1 and Table 2, the (111) lattice parameter increases with the content of Mn shifting the corresponding FCC solid solution peaks towards lower angles. This corresponds to the fact, that Mn has the second-highest atomic radius of 0.161 nm (according to Ref. [39] it is the largest atom in the studied alloy) compared to Co (0.152 nm), Cr (0.166 nm), Fe (0.156 nm), and Ni (0.149 nm).

The observed (111) lattice parameter of the MA + SPS Mn20 alloy was found to be 0.3592 nm, a value situated between that reported by Bai et al. [40] (0.3580 nm) and Wang et al. [39] (0.3605 nm). The lower value was obtained in the case of laser-engineered net shaping in its as-printed state followed by its increase due to a stress-strain relaxation during a 2 h annealing at 673 K. On the other hand, Wang et al. [39] reported a slightly higher value, which was mainly caused by the high energy imposed on the sample during the powder arc-additive manufacturing process. Thus, the observed lattice parameter can be related to the slower heat dissipation of the MA + SPS alloys as in the case of laser-engineered net shaping reported by Bai et al. [40]. In addition to the work of Zhang et al. [41], the lattice parameters of MA + SPS alloys ranging between the reported values might be also influenced by the segregation of Mn on sub-grain boundaries affecting the lattice parameter.

The carbide Cr$_7$C$_3$ formed during the mechanical alloying due to the highest possible supersaturation of C, whose source is the n-heptane acting as PCA, and further grew up while being compacted via SPS. The presence of such carbide is favoured due to the lowest Gibbs free energy that has been calculated using the FactSage® software at a theoretical
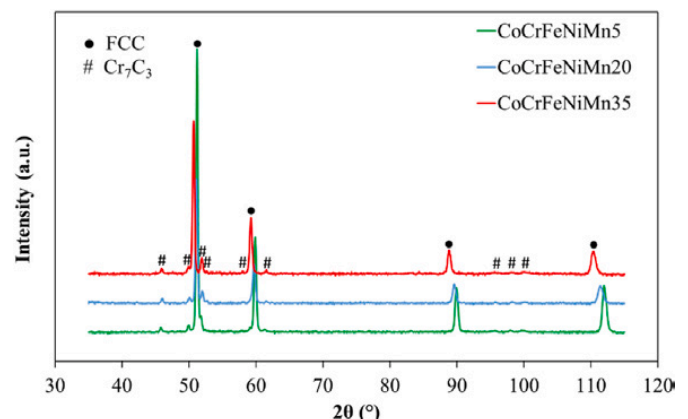

Fig. 1. X-ray diffraction patterns of the MA + SPS alloys.

Table 2
Values of the (111) lattice parameter *a* (nm) for the CoCrFeNiMnX solid solution as a result of Mn content within the alloy.

Sample	CoCrFeNiMn5	CoCrFeNiMn20	CoCrFeNiMn35
a (nm)	0.3577(3)	0.3592(3)	0.3612(7)

Table 4
Quantification of the amount of the Cr_7C_3 phase from XRD patterns of MA + SPS alloys.

Sample	CoCrFeNiMn5	CoCrFeNiMn20	CoCrFeNiMn35
wt.%	6.9	15.1	15.1

temperature of 298.15 K, which is the starting temperature of the mechanical alloying (Table 3). Moreover, it is well known, that the temperature further increases during the alloying process, as well as it is reaching even significantly higher values during the SPS compaction. From this point of view, the presence of Cr_7C_3 is inevitable and may improve, e.g., the tribological properties of these materials. On the other hand, the SiC powder particles, used for reinforcing the alloys are having the lowest absolute value of $\Delta G°$ among possible carbides (Table 3) and so they could serve as another source of carbon within the system due to mutual reactions of this compound with other powder particles that may be possessing a thin layer of oxides on their surface.

The content of the Cr_7C_3 carbide particles, determined by the Rietveld refinement method, is given in Table 4. It was found, that the carbide content was equal in the case of Mn20 and Mn35 alloys reaching up to 15.1%, while the Mn5 alloy had only 6.9%. Since the XRD analysis did not prove the apparent presence of any other carbide except for Cr_7C_3 (admitting only 0.75–1 wt% of $Cr_{23}C_6$ found by TEM in the Mn20 alloy – Fig. 5), there are several reasons for such difference. The first of them could be the mechanical alloying process itself, which is performed in a jar equipped with a pressure relief valve for safety purposes. It is well known, that Fe, Ni, and Co belong to ductile elements while Cr and Mn are rather brittle. Thus, decreasing the content of Mn at the expense of ductile elements may increase the heating-up of the alloying jar in the early beginning due to the increasing influence of friction between the milling balls, powder, and the jar's wall, especially in the early steps of the alloying prior the desired FCC solid solution is formed. One can assume, that the lower content of Mn in the alloy increases the maximal temperature within the jar leading to the increased partial pressure of the PCA, which is then released throughout the pressure relief valve, decreasing in the beginning of the mechanical alloying process the carbon content for carbide formation in the Mn5 alloy.

In the case of alloys with higher Mn amounts (Mn20 and Mn35), reduction of the heating-up due to lower friction allows for higher supersaturation of the newly formed solid solution and formation of a higher amount of Cr_7C_3 carbides. Secondly, the Mn is responsible for the distortion of the crystallographic lattice of the FCC solid solution due to its second largest atomic diameter as has been shown by the change of lattice parameter (Table 2). Therefore, increasing the content of Mn beyond 5 at. % may allow even higher supersaturation of the prepared powders and a formation of a higher amount of carbides during the SPS compaction. Thirdly, according to the work of Zhang et al. [41], the content of Mn seems to be crucial as it segregates on the sub-grain boundaries in HEAs creating accelerated diffusion paths and allowing a rapid formation of the Cr-rich regions and carbides. Nevertheless, such an assumption has not been confirmed accordingly to the TEM + EDS observations of the investigated MA + SPS alloys. The fourth reason could be the substitution of chromium in the carbide by manganese. According to Table 8, the average Cr content in Cr_7C_3 in the Mn5 alloy is

about 50 at.%, and it decreases down to about 40 at.% in the Mn35 alloy, while the Mn content increases from 2 up to 15 at.% in the Mn35 alloy. As a consequence, more of the principal Cr remains available for the Cr_7C_3 formation in Mn20 and Mn35 alloys.

The majority of all the above-mentioned assumptions may compete with each other leading to the formation and growth of carbides during the extremely fast compaction via SPS at 1000 °C, where the sample dwell time is a matter of minutes.

The LM micrographs in Fig. 2 show that the microstructure of the alloys is homogeneous, consisting of fine-grained phases and randomly distributed sub-micron pores regardless the content of Mn within the studied HEAs. The surface area of the pores, determined using the threshold method applied to multiple micrographs of non-etched samples, is ranging from $0.57 \pm 0.05\%$ (Mn5) up to $1.05 \pm 0.14\%$ for the Mn35 alloy (see Table 5).

The observed increase matches the content of thermally stable Cr_7C_3 particles, which wt.% was found the highest in both (Mn20 and Mn35) alloys. Considering this fact, the higher the content of the carbides within the alloy, the more difficult the sintering and overall porosity reduction. This assumption is further confirmed by the lowest porosity of 0.57 ± 0.05 % of Mn5 alloy having the lowest content of Cr_7C_3 (Table 4). Accordingly to the [42], such low porosity might only slightly affect the overall material's properties considering both three approaches, including percolation, linear or Archie's law. Moreover, due to the chosen preparation set-up limiting the sample dimensions for being compressively tested, the negative effect of present pores is even less significant.

A more detailed examination of the prepared compacts has been performed by electron microscopy. From SEM backscattered electron micrographs (Fig. 3a–c) and STEM high-angle annular dark-field (HAADF) micrographs (Fig. 3d–f), it is visible that the alloys differ in the (nanometric) grain size and (dark) oxide particle distribution. From the STEM EDS analysis, it follows, that the most frequent were Mn oxides, followed by Cr_2O_3, SiO_2, Fe oxides, Al_2O_3, NiO and CoO. The quantified microstructure parameters are summarized in Table 6. The Mn20 alloy (Fig. 3b, e) has the finest (FCC matrix + Cr_7C_3) grains (166 nm on average) and SiO_2 particles (7–250 nm in size). With decreasing the Mn content (Mn5 alloy – Fig. 3a–d), the matrix and carbide grains and oxide particle size slightly increased (252 nm, and 50–430 nm, respectively). Increasing the Mn amount (Mn35 alloy – Fig. 3c, f) leads to coarsening matrix and carbide grains (320 nm) and SiO_2 particles (150–600 nm). The observed size difference of the matrix and carbide grains and oxide particles can be directly related to the overall hardness of the alloys, which was found to be the highest in the case of the Mn20 alloy, having the finest microstructural parameters (Table 6). Therefore, the higher the hardness of a prepared alloy, the easier the fragmentation of present phases. The trend in microstructural refinement can be attributed to several factors that make the mechanical alloying process of the CoCrFeNiMn alloy more complex. According to the work of Wong et al. [30], the higher the Mn content within the CoCrFeNiMn alloy, the higher the hardness due to solid solution strengthening and the lowering of stacking fault energy, which makes dislocation cross-slip much more difficult. Thus, the higher the Mn content within the alloy, the easier the fragmentation and microstructural refinement. However, the Mn35 alloy exhibits contrary behavior, as the SiO_2 and FCC matrix grains are the coarsest of all the investigated alloys. This phenomenon can be related to the increasing friction coefficients (see Table 12), which rise with the Mn content. Considering that the friction coefficients were measured using an Al_2O_3 ball, the values would be higher during the

Table 3
Calculated values of the Gibbs free energy for the formation of the most common carbides of used elements at a theoretical temperature of 298.15 K.

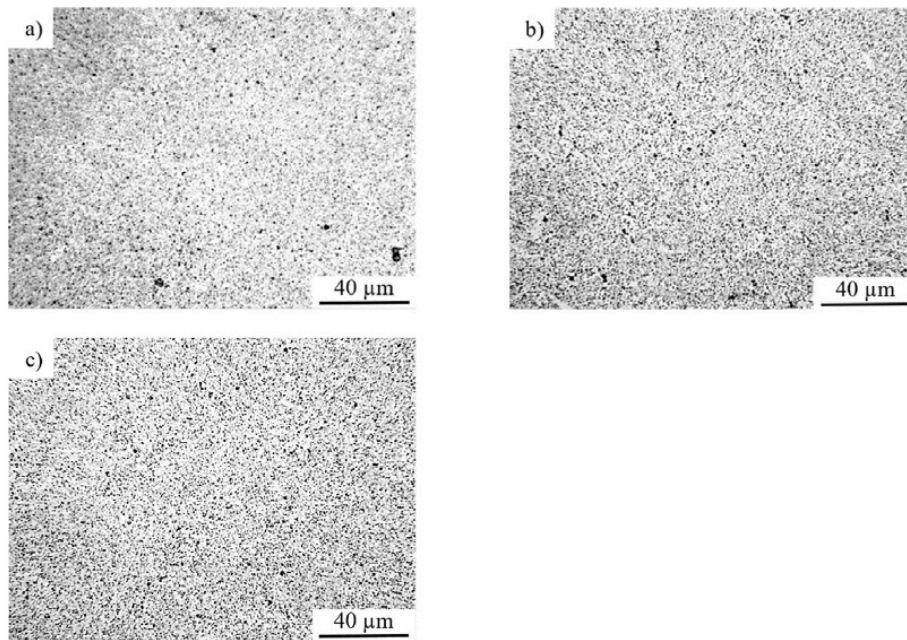| Reaction	Compound	$\Delta G°_{298.15}$ $\left[kJ \, mol^{-1} \right]$
$7Cr + 3C \rightarrow Cr_7C_3$	Cr_7C_3	−2160.5
$3Fe + C \rightarrow Fe_3C$	Fe_3C	−650.2
$3Ni + C \rightarrow Ni_3C$	Ni_3C	−607.2
$3Mn + C \rightarrow Mn_3C$	Mn_3C	−710.7
$Si + C \rightarrow SiC$	SiC	−70.8

Fig. 2. LM micrographs of etched MA + SPS: a) CoCrFeNiMn5; b) CoCrFeNiMn20; c) CoCrFeNiMn35 alloys. *(part of many figures used for further evaluation of the average surface porosity)*.

Table 5
The average surface porosity of the polished compact alloys evaluated using the threshold method on multiple figures of each alloy.

Sample	CoCrFeNiMn5	CoCrFeNiMn20	CoCrFeNiMn35
Area fraction [%]	0.57 ± 0.05	0.93 ± 0.16	1.05 ± 0.14

milling of the alloy within an AISI 420 stainless steel jar. Thus, during the mechanical alloying of the powders, the newly formed alloy increases the friction coefficients in the later stages of the process, causing significant heating of the alloy on a highly localized scale and allowing microstructural coarsening of present phases. More importantly, the coarser the SiO_2 particles become, the less they suppress the further growth of FCC solid solution grains. Based on the local chemical microanalysis of the STEM HAADF micrographs, the appearance of variety grey tones of FCC grains is rather caused by their diffraction
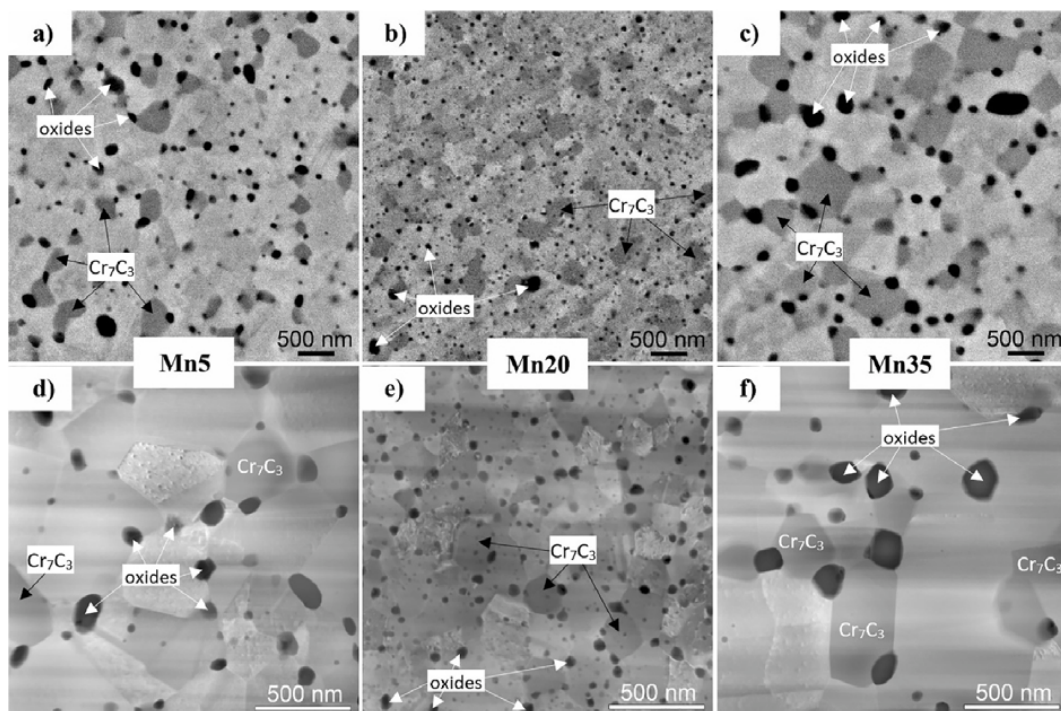

Fig. 3. Electron microscopy micrographs showing grains and particles dispersed in the MA + SPS CoCrFeNiMnX (X = 5, 20, 35 at.%) high-entropy alloys: (a–c) SEM – BSE, (d–f) STEM HAADF.

Table 6

Average matrix and carbide grain size, SiO_2 particle size, and its area fractions determined from SEM and STEM micrographs.

Sample	CoCrFeNiMn5	CoCrFeNiMn20	CoCrFeNiMn35
Grain size (FCC + Cr_7C_3) [nm]	252 ± 21	166 ± 17	320 ± 21
SiO_2 particle size [nm]	50–430	7–250	150–600
SiO_2 area fraction [%]	3.50 ± 0.86	3.10 ± 0.78	4.60 ± 1.59

orientation instead of corresponding to a different Z-contrast.

The added SiC is known as a brittle phase, which can easily undergo fragmentation during the mechanical alloying process. The SiC powder particles further undergo a chemical reaction during the mechanical alloying, forming a more thermodynamically stable SiO_2. Although the

dimensions of SiO_2 particles look a bit different (Fig. 3, Table 6), their area fractions in Mn5 and Mn20 alloys are comparable (3.5 and 3.1 %, respectively) and slightly lower than in the case of the Mn35 alloy (4.6 % - Table 6). It should be noted that the dimensions of the SiO_2 particle scatter show a significantly higher proportion of smaller particles across all the MA + SPS samples. The overall content of such phases (SiC or newly formed SiO_2) is below 5 wt%, so their fractions do not contribute to the XRD pattern in Fig. 1. On the other hand, the Cr_7C_3 carbide particles are coarser (comparable to FCC matrix grains – Fig. 4Fig. 5), and their overall content is significantly higher, as can be seen from Fig. 3 Fig. 4 and also from XRD analysis results (Table 4).

The Gibbs free energy of reactions forming the most common and thermodynamically stable oxide products is shown in Table 7. As is shown, the addition of SiC resulted in its reaction with the residual oxygen, whose source is mainly the pre-oxidized powder particles of
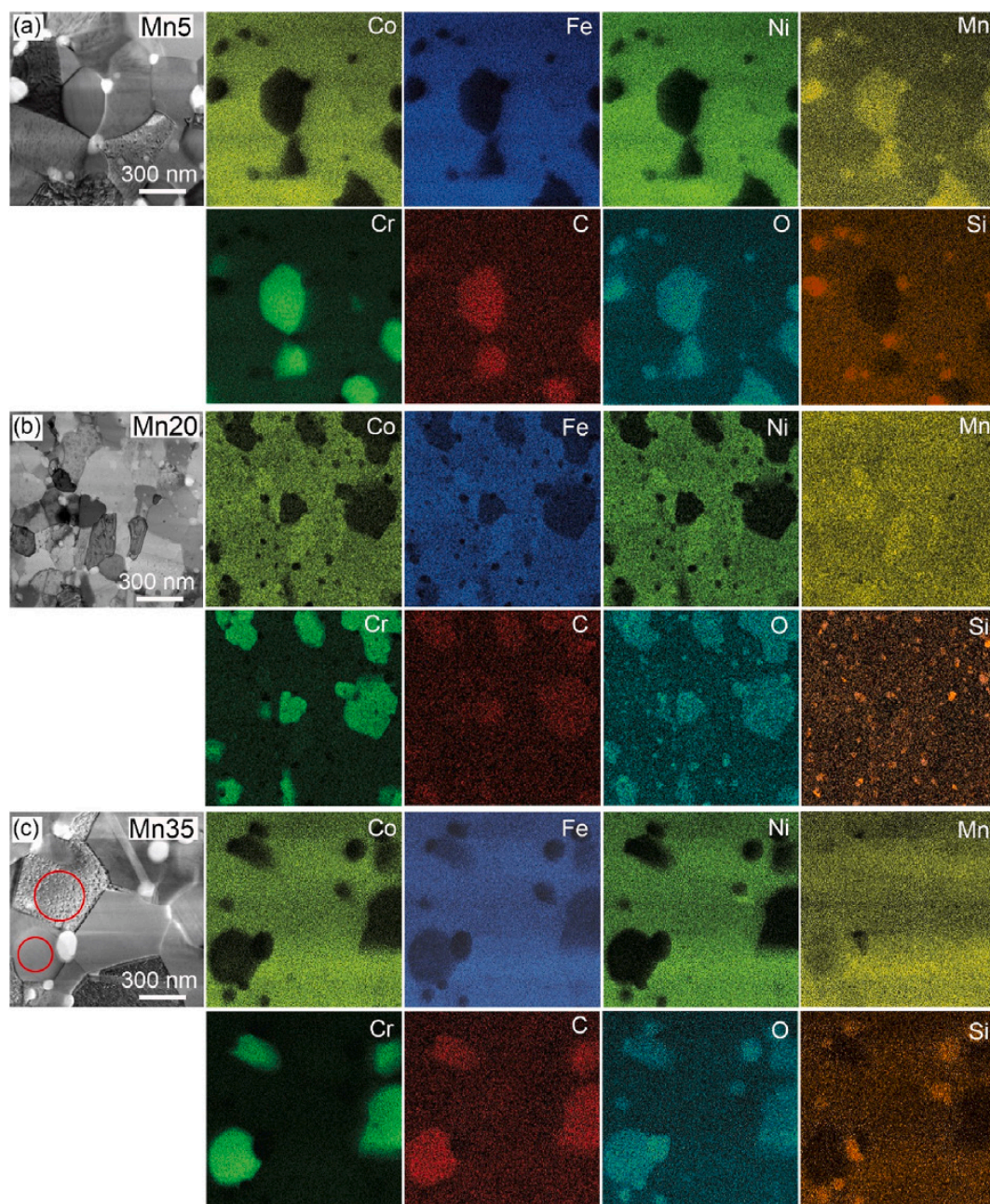

Fig. 4. STEM bright-field (BF) micrographs and EDS maps of the Mn5, Mn20, and Mn35 CoCrFeNiMnX high entropy alloys. *(Red circles in the inset in the micrograph (c) show examples of pop-up areas used for quantification of the chemical composition of the carbide particles and the adjacent matrix from EDS maps – results are in Table 8).* (For interpretation of the references to colour in this figure legend, the reader is referred to the Web version of this article)
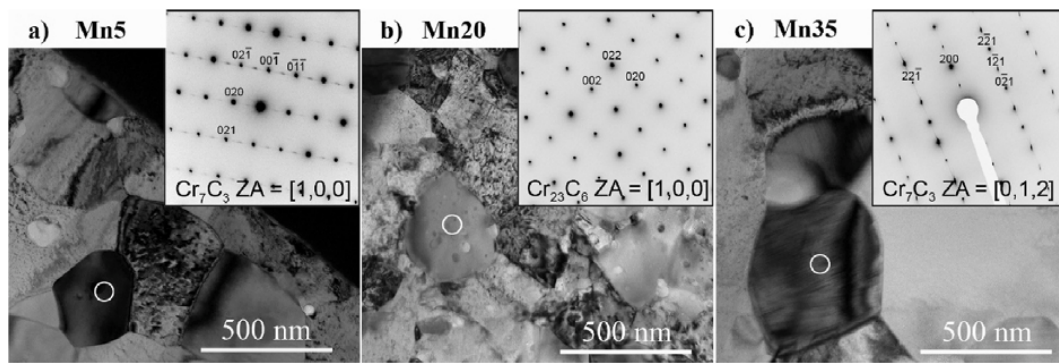
Fig. 5. Bright-field TEM micrographs of chromium carbide particles; the insets show (precession) nanodiffraction patterns obtained in the spots marked by white circles.

Table 7
Calculated values of the Gibbs free energy for the formation of the most common oxides of used elements at a theoretical temperature of 298.15 K.

Reaction	Compound	$\Delta G^{\circ}_{298.15} \; [kJ \bullet mol^{-1}]$
$2Co + O_2 \rightarrow 2CoO$	CoO	−214.02
$3Co + 2O_2 \rightarrow Co_3O_4$	Co_3O_4	−794.96
$4Cr + 3O_2 \rightarrow 2Cr_2O_3$	Cr_2O_3	−1046.66
$2Fe + O_2 \rightarrow 2FeO$	FeO	−244.87
$4Fe + 3O_2 \rightarrow 2Fe_2O_3$	Fe_2O_3	−744.02
$3Fe + 2O_2 \rightarrow 2Fe_3O_4$	Fe_3O_4	−1014.3
$2Ni + O_2 \rightarrow 2NiO$	NiO	−211.75
$2Mn + O_2 \rightarrow 2MnO$	MnO	−362.66
$4Mn + 3O_2 \rightarrow 2Mn_2O_3$	Mn_2O_3	−875.97
$3Mn + 2O_2 \rightarrow Mn_3O_4$	Mn_3O_4	−1281.59
$Si + O_2 \rightarrow SiO_2$	SiO_2	−856.3

Table 8
Average composition of carbide particles and adjacent matrix from EDS maps (at. %).

Sample	Chemical composition (at.%)						
	Co	Cr	Fe	Ni	Mn	C	Si
Mn5							
carbides	**3.87 ± 1.81**	**49.72 ± 5.14**	**6.43 ± 2.48**	**2.27 ± 1.99**	**2.32 ± 0.82**	**34.07 ± 3.52**	**0.72 ± 0.48**
matrix	23.18 ± 0.49	12.95 ± 1.21	26.50 ± 1.09	22.60 ± 1.04	4.66 ± 0.29	7.85 ± 2.85	1.45 ± 0.34
Mn20							
carbides	**4.24 ± 0.65**	**45.60 ± 2.61**	**9.17 ± 0.63**	**2.71 ± 0.72**	**9.71 ± 1.18**	**28.00 ± 4.18**	**0.35 ± 0.24**
matrix	17.43 ± 0.94	11.03 ± 2.54	22.60 ± 1.41	17.19 ± 1.32	17.50 ± 1.52	6.55 ± 4.46	1.99 ± 0.33
Mn35							
carbides	**2.52 ± 1.00**	**40.58 ± 4.47**	**6.74 ± 1.39**	**1.14 ± 0.92**	**15.33 ± 2.13**	**33.34 ± 3.36**	**0.35 ± 0.12**
matrix	18.02 ± 0.23	3.90 ± 0.30	21.74 ± 0.33	18.54 ± 0.33	28.41 ± 0.84	4.15 ± 1.02	2.29 ± 0.11

other elements, forming SiO_2 particles within the alloys. This was favoured since SiO_2 is a more thermodynamically stable Si-based compound, having the fourth-lowest Gibbs free energy, after the Cr and some of the Fe or Mn oxides. However, the later mentioned element tends to create carbides, in which Gibbs free energy is significantly lower (Table 3). The carbides are then formed either during the mechanical alloying or more likely, during the consequential compaction via SPS, where all the sides of compacted powder are in direct contact with graphite shielding foils acting as another additional source of carbon. It should be stressed that the reaction of the initially added SiC leading to a formation of SiO_2 further increases the content of C within the prepared alloy. The reaction was fully completed since there were no traces of remaining SiC within the alloys. Therefore, the SiC could not act as highly localized sources of C, allowing the formation of Cr-based carbides in their vicinity, as was e.g. reported in the work of Shao et al. [43].

Containing a high amount of chromium, the carbides scatter electrons similarly to the CoCrFeNiMnX solid solution, and so they cannot be reliably distinguished from the matrix grains (Fig. 4). However, from the EDS maps (Fig. 4), it follows that they are coarser than the oxidic particles, having 100–600 nm in size in all three alloys. Furthermore, their fraction is much higher (ranging from 6.9 to 15.1 wt%, Table 4) than the oxidic particles (3.5–4.6 %, Table 4). STEM EDS mapping has been exploited to obtain not only a qualitative distribution of elements in the microstructure but also to quantify the composition of the carbide particles and the adjacent CoCrFeNiMnX matrix. The average values, obtained from at least 9 measurements (pop-up areas marked in Fig. 4c) on several EDS maps of the investigated MA + SPS alloys, are summarized in Table 8.

Detailed results show that the present carbides, identified by the X-ray diffraction analysis as Cr_7C_3, are showing substitution by the remaining elements, among which the Fe is in the Mn5 alloy having its highest content. The content of Mn within the present carbide increases

with the alloy's actual chemical composition overcoming the Fe and finally reaching up to 15.3 ± 2.1 at.% (Table 8). The observed mutual substitution of Cr by other elements is achieved due to the almost similar (Mn) or smaller atomic radii of the remaining atoms. Therefore, the present carbides shall be rather mentioned as M_7C_3 (M = Cr, Co, Fe, Ni, Mn). The presence of carbides within the HEAs can be sometimes interchanged with the Cr-enriched phases, which occurrence was also confirmed in a variety of CoCrFeNi-based alloys accordingly to the work of others [44–48], identifying it as the σ phase. However, considering the possibilities of experimental equipment back in the days, these phases might be in some works [46,47] wrongly identified without in-depth TEM investigations. Therefore, in a presence of a carbon-bearing environment, it is highly likely the carbides are preferentially formed, as was also confirmed by the work of Christofidou et al. [49] describing the precipitation of carbides within the arc-melted materials.

Both the M_7C_3 carbide and σ phase are reported to have different influences on the properties of the materials, and their presence might be either beneficial (Cr_7C_3) or highly deleterious (σ phase) as in the case of duplex steels [50]. The influence of each phase can be demonstrated e.g., on their hardnesses or thermal stability, both significantly higher in the case of Cr_7C_3 reaching HV up to 17 GPa (18.3 GPa calculated) [51], while being thermally stable up to a temperature range of 1290–1315 °C [52]. In comparison, Laplanche et al. [44] described the stability of the σ

phase up to a temperature of ~1070 °C, which might be a sufficient temperature to dissolve the σ phase in the investigated MA + SPS alloys during the SPS compaction at 1000 °C (overheating on the top of the compacted sample is reaching up to 1035–1037 °C). The Cr-enriched phases were showing, compared to the results given in Ref. [44], extremely low content of other elements. In addition, the matrix grains corresponding to an FCC solid solution were consequently depleted in Cr, as is also reported in Refs. [44,53]. Compared to the previously mentioned works, the adjacent FCC matrix of the MA + SPS alloys showed far more extreme depletion of Cr reaching less than one-third of the concentration of the Cr content within the carbide (Table 8). Moreover, the Cr depletion further increases with the content of Mn, reaching for the Mn35 alloy 40.58 ± 4.47 at.% Cr while the surrounding matrix contained only 3.90 ± 0.30 at.% of Cr. This difference was caused by the preparation processes, among which the mechanical alloying shall be considered a non-equilibrium method compared to e.g., induction melting used in the formerly mentioned research [44,53]. In addition, the content of Fe reached higher values, compared to the intended chemical composition of each alloy, which was caused by the contamination by the jar material.

The presence of the M_7C_3 carbides was also verified by electron (precession) nanodiffraction (patterns as insets in Fig. 5). All the investigated alloys contained orthorhombic M_7C_3 carbides, although a few individual particles identified as $M_{23}C_6$ carbides, were found in the Mn20 alloy. The $M_{23}C_6$ carbide is a transitional chromium carbide preceding the formation of a more stable M_7C_3 [54]. Its presence confirmed the X-ray diffraction results, although stating a total amount of them to be up to 1.0 wt%. According to the electron nanodiffraction, the *c* parameter of the crystallographic lattice of several examined M_7C_3 particles was a little lower (0.4386 nm) when compared to JCPDs 36–1482 file, used for X-ray diffraction identification (from where $a = 0.701$ nm, $b = 1.2142$ nm, $c = 0.4526$ nm). This change could be attributed to the substitution of Cr in the carbide by other elements in the alloy and namely by the local character of the measurement (the actual composition of the particle could be different from the average values given in Table 7).

The presence of M_7C_3 carbides was reported throughout a variety of works preparing the CoCrFeNiMn-based alloys via additive manufacturing [35,39], mechanical alloying and vacuum hot pressing [55,56], isostatic pressing [57] or spark plasma sintering [58], compaction of the already prepared alloy and its sintering at elevated temperature [43] or by a combination of aforementioned techniques, e. g. gas atomization followed by mechanical alloying and spark sintering. More importantly, the formation of this phase is not affected by Mn, although its content was found to be growing the most, reaching up to 15.33 ± 2.13 at.% for the Mn35 alloy (Table 8). Therefore, although the formation of the Cr_7C_3 carbide is not related to the presence of Mn, it actively dissolves Mn within it. This can be further confirmed by the work of Sathiyamoorthi et al. [58] who prepared quinary CoCrFeNi alloy via a combination of MA + SPS also confirming the presence of Cr_7C_3 phase, which starts to slowly dissolve in the FCC matrix at 1000 °C and completely disappears above 1200 °C. As can be assumed from the work of Rogal et al. [57], the preferential formation of $Cr_{23}C_6$ in the CoCrFeNiMn alloys changes with the addition of SiC favouring the formation of the Cr_7C_3 phases. This corresponds to our observations, where the later mentioned carbides were identified. Moreover, one can assume, that the higher speed/energy of the mechanical alloying also significantly contributed to the stabilization of Cr_7C_3 since the amount of residual $Cr_{23}C_6$ phase was found to be extremely low.

3.2. Mechanical properties

All the MA + SPS alloys were investigated for their mechanical properties, including hardness and compressive stress-strain properties. As shown in Table 9, the highest hardness of 392 ± 9 HV 30 was achieved in the case of equiatomic CoCrFeNiMn20 alloy. Other than the

Table 9
Vickers hardness (HV 30), instrumented (HV_{IT}) microhardness, and elastic modulus (E_{IT}) of studied alloys.

Sample	CoCrFeNiMn5	CoCrFeNiMn20	CoCrFeNiMn35
HV 30	325 ± 4	392 ± 9	331 ± 5
HV_{IT} 1	399.4 ± 3.7	475.6 ± 2.5	416.0 ± 7.3
E_{IT} [GPa]	199.6 ± 12.4	193.8 ± 3.3	190.1 ± 10.8

equiatomic composition resulted in a hardness decrease reaching its minimum of 325 ± 4 HV 30 for the CoCrFeNiMn5 alloy. This confirms that the hardness of the alloys is foremostly Hall-Petch grain-size dependent (see Table 6) compared to the weak dependence on the actual chemical composition. This corresponds similarly to the results of mechanically alloyed and hot isostatic pressed CoCrFeNiMn$_x$ (X = 0.5, 1.0, 1.5, 2.0, 2.5, 3.0) [32] or on a group of CoCrFeNi-based alloys prepared by arc melting [38]. Accordingly, the highest hardness of 392 ± 9 HV 30 was achieved in the case of Mn20 alloy, having the smallest grain size of 166 ± 17 nm (Table 6). Among the Hall-Petch contribution, the presence of SiO_2 and especially of Cr_7C_3, the latter mentioned having the highest volume fraction, further increased the hardness of the prepared MA + SPS alloys, which can be confirmed by the second highest HV 30 for Mn35 alloy. In this case, the microstructure was coarser, while having a comparable amount of carbides and a slightly higher content of SiO_2 reaching up to $4.60 \pm 1.59\%$ (Table 6).

The instrumented (IT – loading-unloading) Vickers microhardness measurements using a 1 kg load confirmed the HV 30 results showing the superior hardness of Mn20 alloy reaching up to 475.6 ± 2.5 HV_{IT} 1. The observed hardness of the prepared alloys is superior to values reported in the work of Min et al. [59], whose equiatomic CoCrFeNiMn single-phased alloy achieved a hardness of only 183 ± 4 HV. The equiatomic CoCrFeNiMn alloy of Mehranpour et al. [12] prepared by arc melting and consequentially rolled at room (25 °C) or even cryogenic (−190 °C) temperatures reaching a total thickness reduction of 28 or 55% did not exceed the hardness values of alloys reported here. However, exceeding the equivalent strain of 1.4 of the cold-rolled equiatomic alloy resulted in a hardness of 450 ± 10 HV [60] and remained almost constant even at a strain equivalent of 4.2. Therefore, the samples reached certain saturation at a hardness value similar to the hardness of the MA + SPS equiatomic alloy. In addition, the hardness of all the MA + SPS alloys is also superior to 157.1 HV1 of additively printed one [61]. Furthermore, the hardness and overall mechanical properties might increase by a thermal treatment that may result in the formation of precipitates finely dispersed within the FCC matrix. This might be favoured, based on the observations made in Ref. [62], due to the large content of lattice defects as a consequence of the intensive plastic deformation, which is common for both rolling and MA. The instrumented (IT – loading-unloading) Vickers microhardness measurements using a 1 kg load shows the same trend as HV30 results even if it reaches higher hardness values. The observed increase is probably a consequence of different methods used for data processing and probing of different volumes of the material. While the residual imprint is measured optically after the complete unloading for the traditional Vickers hardness, instrumented values are calculated from the unloading part of the indentation depth-force curve [63]. This is the reason, why the values of the traditional Vickers hardness usually slightly differ from the values obtained by instrumented technique. Besides these differences in the evaluation process, the smaller size of the probed volume and indentation size effect [64] can be the reason for the higher values obtained by instrumented technique. Elastic modulus E_{IT} (Table 9) slightly decreases with the increasing Mn content while being still in good agreement with the literature data for Cantor alloy [65–67].

The compressive stress-strain test was carried out at laboratory temperature (LT) on the as-compacted samples as well as on those annealed for 100h at 800 °C and also at elevated temperatures of 600 and 800 °C. The corresponding curves are shown in Fig. 6, while the

average compressive yield strength (CYS) values are summarized in Table 10. According to the results in Fig. 6a and Table 10, the highest CYS of 1024 ± 17 MPa was achieved for the Mn20 alloy. Considering the effect of Mn content, non-equiatomic compositions (Mn5 and Mn35) resulted in a decrease in the CYS values (Table 10) while the ductility of both alloys increased (Fig. 6a). Both the non-equiatomic alloys tested at LT in the as-compacted condition (Fig. 6a), and after annealing for 100 h at 800 °C (Fig. 6b), exhibited continual strain hardening without any traces of cracks initiation up to strains of 38%. On the other hand, the equiatomic Mn20 alloy reached at laboratory temperature somewhat lower total strains of approximately 33 % and ultimate compressive strength (UCS) of 2153.7 ± 32.4 MPa, or 28 % and 1847.8 ± 34.6 MPa for the samples annealed at 800 °C for 100h, respectively. The MA + SPS alloys exhibit far higher CYS and UCS at laboratory temperature compared to the mechanically alloyed CoCrFeNiMn alloy reported by Zhang et al. [59], reaching CYS of 228 MPa and UCS >946 MPa. Considering the ultrafine-grained character of the microstructure, the MA + SPS alloys also significantly outperformed the properties of gas atomized and vacuum hot-pressed equiatomic alloy reaching CYS of only 212 MPa and UCS >968 MPa [59]. The main reason for such distinctive behaviour is the presence of a large number of refined SiO_2 particles (see Fig. 3 Fig. 4), which effectively hinders grain deformation. Although the area fraction (see Table 6) of the oxide particles is the lowest, their finest dimensions together with the dimensions of the matrix grains are the main reason for achieving the lowest, yet still sufficient ductility. In addition, the negative contribution of the porosity (Table 5) on the ductility of the Mn20 alloy seems to be negligible since it is lower (0.93 ± 0.16%) compared to the Mn35 alloy (1.05 ± 0.14%). In comparison, Yim et al. [36] achieved in the case of induction-melted and water-atomized powders that further underwent short-term mechanical milling significantly lower CYS of only 508 MPa. Furthermore, even the alloying with TiC [36] forming a sort-of composite alloy increased the CYS up to 698 MPa and still did not outperform the

Table 10
Summary of the average CYS values [MPa] of studied alloys. *(LT – laboratory temperature)*.

Sample	CoCrFeNiMn5	CoCrFeNiMn20	CoCrFeNiMn35
LT	919.1 ± 12.1	1024.1 ± 17.8	879.3 ± 16.5
LT (100h at 800 °C)	884.2 ± 12.8	956.3 ± 35.2	793.0 ± 15.9
at 600 °C	714.8 ± 2.2	649.4 ± 10.5	603.6 ± 1.8
at 800 °C	189.8 ± 33.0	114.9 ± 0.8	80.3 ± 5.8

properties of the MA + SPS alloys reported in our work. This points out the high importance of the microstructural features, especially in the dimensions of the present phases, among which the FCC grain sizes reported in Ref. [36] were 10.6 μm and further become refined as the TiC was added to the system down to 5.1 μm. This is a tremendous difference from the dimensions of particular phases found in the investigated MA + SPS alloys where the largest FCC grain sizes of the Mn35 alloys were 320 ± 21 nm (Table 6), and then become even finer.

The investigated alloys were also compressively tested at LT after being exposed to 800 °C for a total dwell time of 100 h. As is shown in Fig. 6b, the observed alloys showed good thermal stability reducing their CYS (Table 10) accordingly to the increasing content of Mn. Such behaviour can be associated with the ultrafine-grained nature of the FCC matrix grains, which coarsening is on one hand effectively hindered either by the present Cr_7C_3 and/or foremostly by the nanocrystalline SiO_2 particles. This effect is evident by the increasing reduction of the CYS, which can be matched with the overall content of SiO_2 and their dimensions within the material (Table 6). On the other hand, as the content of Mn increases the diffusion-related processes result in accelerated microstructural coarsening, which works against the barrier effect of the previously mentioned particles. Therefore, the lowest CYS decrease of ~35 MPa is achieved in the case of Mn5 alloy. As the content of Mn increases, so does the CYS reduction reaching up to ~68 and ~87
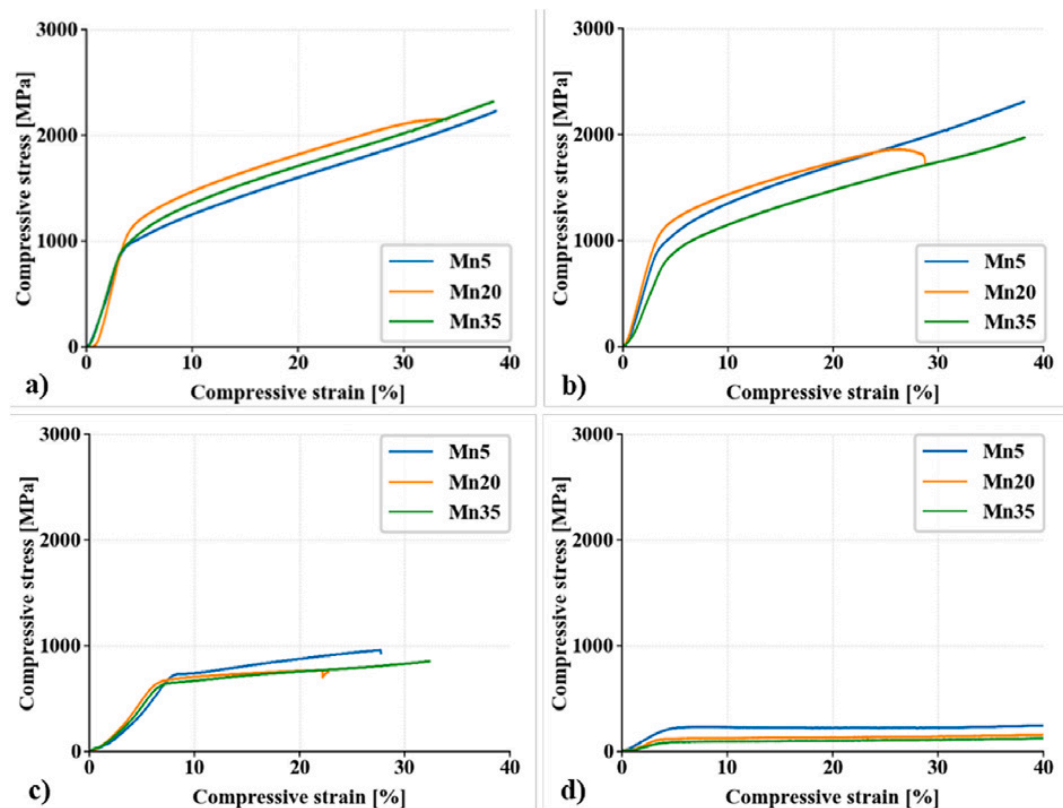

Fig. 6. Compressive stress-strain curves of the CoCrFeNiMnX (X = 5, 20, 35 at.%) alloy performed at: a) laboratory temperature (LT); b) LT after 100 h annealing at 800 °C; and at elevated temperatures of c) 600 °C; d) 800 °C.

MPa for the Mn20 and Mn35 alloys, respectively. Since the tests were done at 800 °C, the present Cr_7C_3 particles were retained within the microstructure, a similar finding that has been made by Sathiyamoorthi et al. [58] confirming their thermodynamical stability up to 1000 °C, after which they start to dissolve slowly. This also confirms the properly chosen conditions of the SPS compaction, which allows obtaining samples nearly the theoretical density while the beneficial appearance of the microstructure is retained due to the presence of carbides/other particles.

The compressive stress-strain tests were performed also at elevated temperatures of 600 °C and 800 °C to determine the positive effect of oxide dispersion strengthening via SiO_2 particles. As is shown in Fig. 6c, all the prepared MA + SPS alloys exhibited at 600 °C comparable behaviour; the CoCrFeNiMn5 alloy reached the highest CYS of 714.8 ± 2.2 MPa, also showing the highest strain hardening rate compared to the remaining alloys. Such behaviour can be related to a significantly lower content of carbide particles within the Mn5 alloy, thus theoretically higher content of C within the FCC solid solution hinders the dislocation movement at a temperature of 600 °C. On the other hand, the CoCrFe-NiMn20 alloy exhibited the second highest CYS of 649.4 ± 10.5 MPa (Fig. 6c–Table 10), outperforming by almost 50 MPa the CYS of non-strengthened, yet identical alloy reported in our previous work [37]. All the MA + SPS alloys tested at a temperature of 800 °C showed an increasing reduction of their CYS following the content of Mn. From this point of view, the lowest the content of Mn, the better the CYS reaching its maxima of 189.8 ± 33.0 MPa for the Mn5 alloy. The observed behaviour can be associated with the stress-strains in the crystallographic lattice, affecting the dislocation mobility, which increases with the content of Mn due to its second largest atomic radii, as was reported earlier. This presumption can be further confirmed by the dimensions of present phases where the MA + SPS Mn5 alloy had average dimensions of each structural constituent, including the FCC grains, carbides, and SiO_2 particles, whose area fraction was also average compared to other alloys.

The herein-reported results can be compared with the work of others, reinforcing the equiatomic CoCrFeNiMn via variety of particles (Table 11). From this point of view, all of these reported significantly higher content of reinforcing particles, ranging from 3 wt% and going up to several tens of wt.%. Comparing these data, all the MA + SPS alloys were showing higher YS values, compared e.q. to the alloy reinforced by up to 20 wt% of Cr_3C_2 particles, which corresponds to multiple times higher content than in the investigated MA + SPS alloys. Among that, the hardness values are similar or slightly lower compared to the rest of the reported alloy systems being significantly more reinforced.

The results of the wear measurements done in a linear mode are shown in Table 12. As one can see, the specific wear rate coefficient (W_s)

was similar for all the tested alloys while showing its minima of $3.54 ± 0.09 \times 10^{-4}$ mm^3 N^{-1} m^{-1} in the case of the Mn5 alloy. Increasing the content of Mn resulted in a higher W_s reaching $6.34 ± 0.60 \times 10^{-4}$ mm^3 N^{-1} m^{-1} for the Mn20 alloy, a value that is, accounting for the standard deviation, comparable to 5.60×10^{-4} mm^3 N^{-1} m^{-1} reported in Ref. [69]. It should be noted that according to the work of Zhang et al. [72], the W_s of the identical equiatomic HEA is the highest when using an Al_2O_3 sliding ball, while it becomes the lowest for the ball made of Si_3N_4. According to that, the W_s can differ from $4.307 ± 0.215 \times 10^{-4}$ mm^3 N^{-1} m^{-1} (for Al_2O_3) to $1.339 ± 0.109 \times 10^{-4}$ mm^3 N^{-1} m^{-1} (for Si_3N_4). Therefore, the above-mentioned W_s of 5.60×10^{-4} mm^3 N^{-1} m^{-1}, measured by Guo et al. [69] using a Si_3N_4 ball, shall be much higher when measured using Al_2O_3, which confirms the W_s superiority of the MA + SPS Mn20 alloy reinforced with SiO_2 particles.

On the other hand, the highest W_s was observed in the case of the MA + SPS Mn35 alloy. These results followed the increasing friction coefficient as a consequence of the Mn content in the alloy reaching its maxima of 0.726 for the MA + SPS Mn35 alloy (Table 11). This behaviour is a result of high tangential forces between the sliding ball and tested materials. This allows highly localized overheating and localized microplastic deformation associated with oxidative wear generating the oxide particles, which are concentrated especially at the wear track heads (as shown in Fig. 7). Considering the average friction coefficient values, the Mn5 alloy shows the lowest friction coefficient of 0.666, which was probably achieved by a mutual effect of matrix softening and oxide lubrication. This presumption is further supported by the presence of a significantly smaller amount of oxidic particles found on the wear tracks head of the Mn5 alloy as is shown in Fig. 7. This supports the presumption of oxide lubrication without significant spalling. Among that, the wear tracks of all the MA + SPS alloys showed the presence of grooves caused by the debris and oxide particles entrapped within the tested material. Especially, the grooves became quite deep in the case of Mn35 alloy, having the broadest SiO_2 particle size ranges that vary between 150 and 600 nm (Table 6).

Comparing the wear track profiles shown in Fig. 8, all the tested alloys showed signs of plastic deformation forming small protrusions on

Table 12

Results of linear mode wear experiments showing the surface roughness (R_a), specific wear rate (W_s) and friction coefficients.

Sample	CoCrFeNiMn5	CoCrFeNiMn20	CoCrFeNiMn35
R_a [μm]	0.008	0.022	0.015
W_s [x10^{-4} mm^3 N^{-1} m^{-1}]	3.54 ± 0.09	6.34 ± 0.60	7.32 ± 0.60
Friction coefficient	0.666	0.712	0.726

Table 11

Comparison of the mechanical properties at LT of the MA + SPS alloys reinforced by ~ 1.8 wt% SiO_2 with other equiatomic CoCrFeNiMn alloys. *(MA – mechanical alloying; SPS – spark plasma sintering; HIP – hot isostatic pressing; WA – water atomization; GA – gas atomization; HPT – high pressure torsion; AN – annealed).*

| Alloy	Reinforcing particles	wt.%	Processing	Hardness	YS at LT (MPa)	Ref.
CoCrFeNiMn5	SiO_2	≈1.8	MA + SPS at 1000 °C	325 HV 30/399 HV$_{IT}$ 1	919	this work
CoCrFeNiMn20	SiO_2	≈1.8	MA + SPS at 1000 °C	399 HV 30/438 HV$_{IT}$ 1	1024	
CoCrFeNiMn35	SiO_2	≈1.8	MA + SPS at 1000 °C	331 HV 30/416 HV$_{IT}$ 1	879	
CoCrFeNiMn20	Al_2O_3	5	MA + HIP at 1000 °C/15 min	545 HV	1600	[68]
	Cr_3C_2	10	SPS at 1050 °C	323 HV	578	[69]
	Cr_3C_2	20	SPS at 1050 °C	417 HV	713	
	Cr_3C_2	40	SPS at 1050 °C	682 HV	2045	
	TiC	5	WA + MA + SPS	–	698	[36]
	TiC	5	GA + MA + HPT	626 HV	–	[70]
	TiC	5	GA + MA + HPT + AN 700 °C/1h	450 HV	–	
	TiC	5	GA + MA + HPT + AN 800 °C/1h	390 HV	–	
	TiC	5	GA + MA + HPT + AN 900 °C/1h	300 HV	–	
	SiC	5	MA (100 rpm) + HIP at 1000 °C/15min	485 HV	1480	[57]
	SiC	5	MA (200 rpm) + HIP at 1000 °C/15 min	699 HV	≈1900	
	Y_2O_3	3	MA + SPS at 1000 °C	547 HV (5.36 GPa)	–	[71]
	Y_2O_3	3	MA + SPS at 1000 °C + AN at 900 °C/5h	526 HV (5.16 GPa)	–	
	Y_2O_3	3	MA + SPS at 1000 °C + AN at 900 °C/10h	544 HV (5.33 GPa)	–	
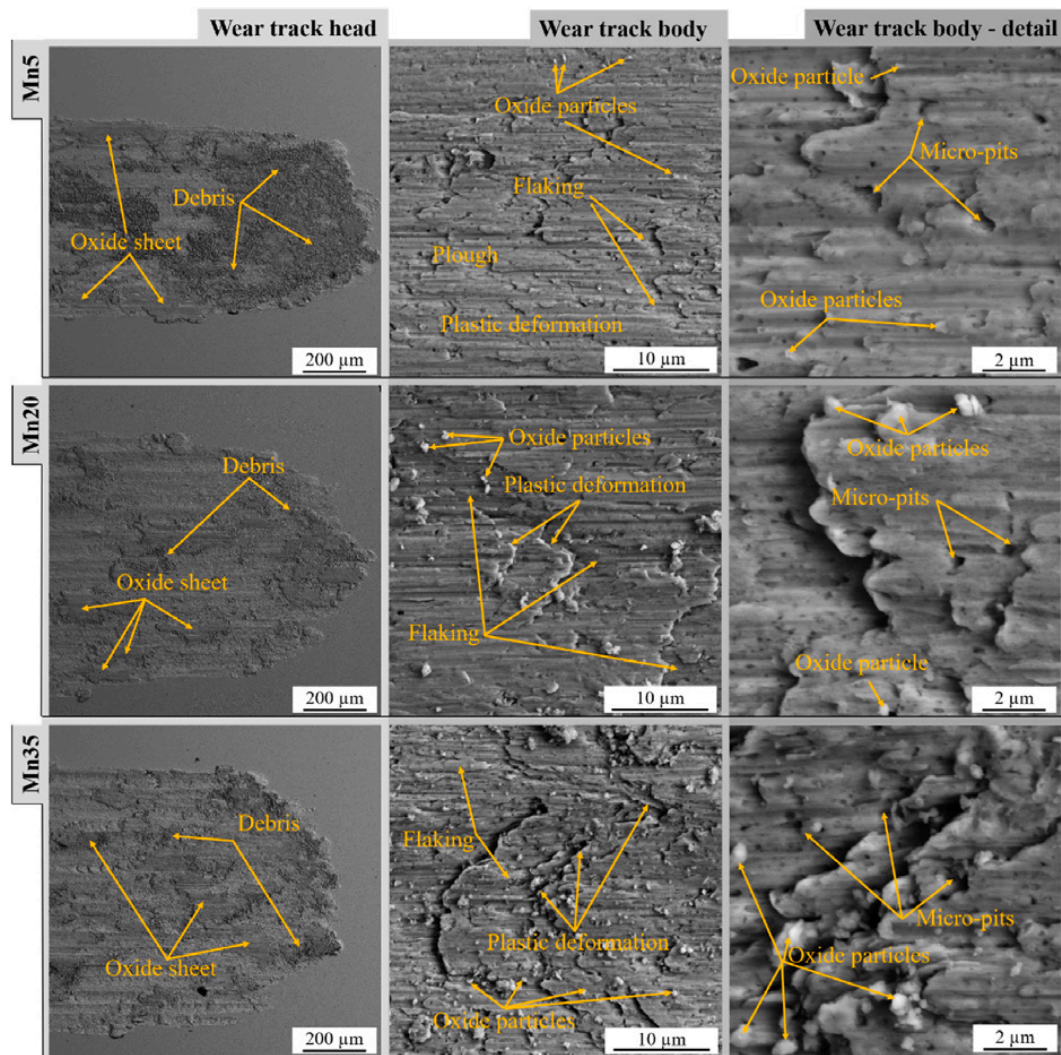
Fig. 7. SEM micrographs of the wear track head of the studied alloys (SE signal).

the edges of the wear track. Among that, the wear tracks showed evidence of delamination due to flaking. In addition, the overall wear track appearance changed as the content of Mn shifted from 20 at.% towards lower or higher contents. From the initially wide track of ≈0.9 μm in width, it transformed into narrower, showing the presence of local grooves caused by ploughing the released particles enhancing the three-body abrasion and inflicting deep grooves into the wear track, as is shown especially in the Mn35 alloy. The wear mechanism comprised abrasive and adhesive contributions with evident signs of oxidative wear speeding up the wear rate. Furthermore, friction-induced heating of the wear track enhanced the microplastic deformation increasing the sub-surface stresses resulting in microscopic fatigue wear. This manifested itself by the creation of micro-pits, as well as flaking pits distributed over the wear track body, as shown in Fig. 7.

The SEM + EDS element maps (Fig. 9) of the wear track revealed the presence of randomly distributed carbides, as well as oxides. Except for the presence of Cr-based carbides, which presence might contribute to the reduction of friction coefficients, a significant content of oxygen was found within the wear track. More detailed SEM + EDS element distribution maps revealed not only the presence of oxygen but also a formation of distinctive oxidic particles that were either accumulated on the wear track heads (Fig. 7) or randomly dispersed in the form of micrometre particles within the wear track. This confirms the above-stated presumption of a high-temperature/oxidative wear mechanism and corresponds to the findings of others [69], confirming the

tribo-oxidation wear mechanism in similar alloys. These particles were present across all the investigated alloys regardless of the amount of Mn.

4. Conclusions

The MA + SPS CoCrFeNiMnX alloys reinforced with SiO_2 particles were mainly composed of FCC solid solutions and carbides being identified in the majority of cases as Cr_7C_3. The amount of carbides, partially substituted by other elements, increased with the Mn content starting from 6.9 wt% (Mn5 alloy) and reaching up to 15.1 wt% for Mn20 and Mn35 alloy. Furthermore, an in-situ reaction of the initially used SiC reinforcing particles resulted in the formation of homogeneously dispersed SiO_2 particles. These particles, as well as the of the FCC solid solution grain sizes varied, reaching its lowest dimensions for the Mn20 alloy, which also exhibited the best mechanical properties, reaching the highest hardness and CYS values at laboratory temperature. On the other hand, the lower the Mn content, the better the performance when tested at 600 and 800 °C due to suppressing the dislocation gliding. Regarding the wear behaviour, all the tested MA + SPS alloys showed a mixed abrasive-adhesive wear mechanism with the occurrence of oxidative wear.

Data availability statement

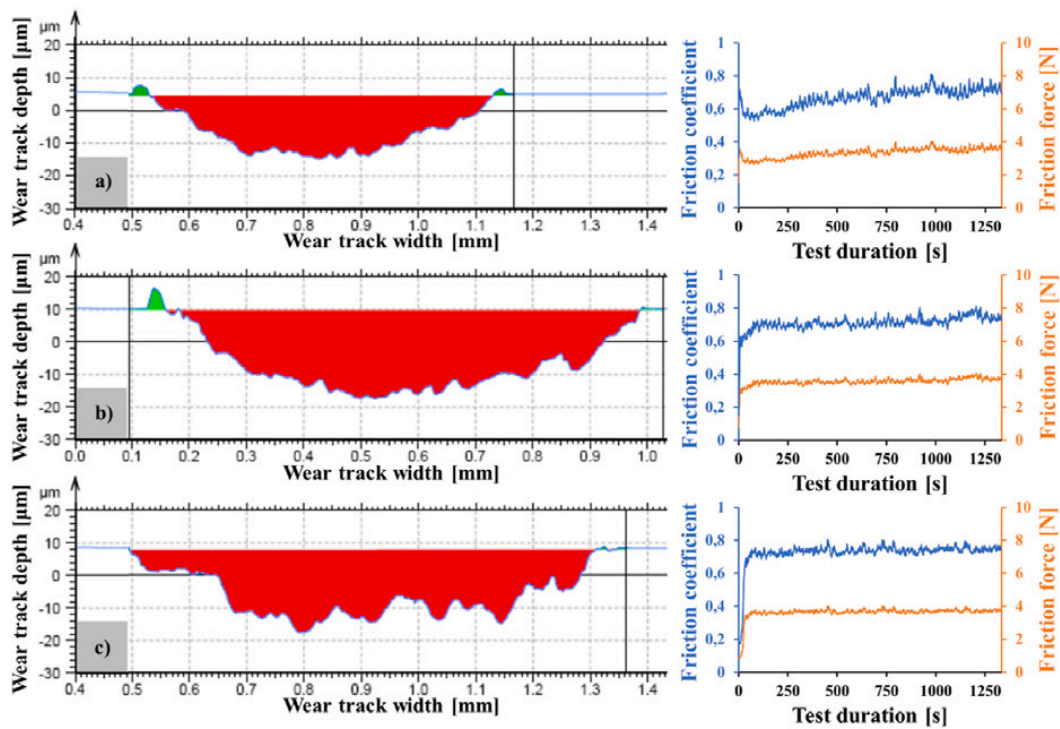The date used in this article are accessible through https://doi.

Fig. 8. Wear track profiles, friction coefficients and friction forces of the: a) CoCrFeNiMn5; b) CoCrFeNiMn20; c) CoCrFeNiMn35 alloys.
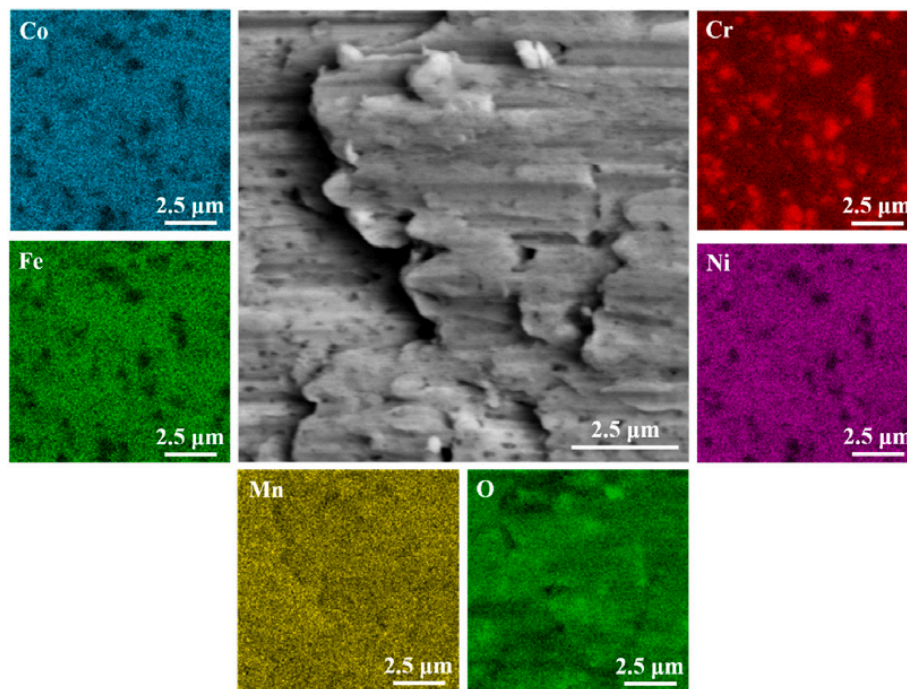

Fig. 9. SEM SE micrograph and corresponding scaled EDS elemental maps within the wear track of the CoCrFeNiMn20 alloy.

org/10.5281/zenodo.10819404.

Declaration of competing interest

The authors declare that they have no known competing financial interests or personal relationships that could have appeared to influence the work reported in this paper.

References

[1] Yeh JW, et al. Nanostructured high-entropy alloys with multiple principal elements: novel alloy design concepts and outcomes. Adv Eng Mater 2004;6(5):299–303.

[2] Miracle DB, Senkov ON. A critical review of high entropy alloys and related concepts. Acta Mater 2017;122:448–511.

[3] George EP, Curtin WA, Tasan CC. High entropy alloys: a focused review of mechanical properties and deformation mechanisms. Acta Mater 2020;188:435–74.

[4] Chang X, et al. Phase engineering of high-entropy alloys. Adv Mater 2020;32(14):1907226.

[5] Otto F, et al. The influences of temperature and microstructure on the tensile properties of a CoCrFeMnNi high-entropy alloy. Acta Mater 2013;61(15):5743–55.

[6] Cantor B, et al. Microstructural development in equiatomic multicomponent alloys. Mater Sci Eng, A 2004;375–377:213–8.

[7] Gali A, George EP. Tensile properties of high- and medium-entropy alloys. Intermetallics 2013;39:74–8.

[8] Laplanche G, et al. Microstructure evolution and critical stress for twinning in the CrMnFeCoNi high-entropy alloy. Acta Mater 2016;118:152–63.

[9] Ma X, et al. Microstructure and mechanical properties of cold drawing CoCrFeMnNi high entropy alloy. J Alloys Compd 2019;795:45–53.

[10] Li Z, et al. Effect of annealing temperature on microstructure and mechanical properties of a severe cold-rolled FeCoCrNiMn high-entropy alloy. Metall Mater Trans 2019;50(7):3223–37.

[11] Gu J, et al. Regulating the strength and ductility of a cold rolled FeCrCoMnNi high-entropy alloy via annealing treatment. Mater Sci Eng, A 2019;755:289–94.

[12] Mehranpour MS, et al. Upgrading of superior strength–ductility trade-off of CoCrFeNiMn high-entropy alloy by microstructural engineering. Materialia 2022;22:101394.

[13] Mehranpour MS, Shahmir H, Nili-ahmadabadi M. CoCrFeNiMn high entropy alloy microstructure and mechanical properties after severe cold shape rolling and annealing. Mater Sci Eng, A 2020;793:139884.

[14] Shahmir H, et al. Effect of annealing on mechanical properties of a nanocrystalline CoCrFeNiMn high-entropy alloy processed by high-pressure torsion. Mater Sci Eng, A 2016;676:294–303.

[15] Shahmir H, et al. Microstructure and properties of a CoCrFeNiMn high-entropy alloy processed by equal-channel angular pressing. Mater Sci Eng, A 2017;705:411–9.

[16] Sathiaraj GD, Bhattacharjee PP. Effect of starting grain size on the evolution of microstructure and texture during thermo-mechanical processing of CoCrFeMnNi high entropy alloy. J Alloys Compd 2015;647:82–96.

[17] Ji W, et al. Alloying behavior and novel properties of CoCrFeNiMn high-entropy alloy fabricated by mechanical alloying and spark plasma sintering. Intermetallics 2015;56:24–7.

[18] Rogachev AS, et al. Structure and properties of equiatomic CoCrFeNiMn alloy fabricated by high-energy ball milling and spark plasma sintering. J Alloys Compd 2019;805:1237–45.

[19] Salishchev GA, et al. Effect of Mn and V on structure and mechanical properties of high-entropy alloys based on CoCrFeNi system. J Alloys Compd 2014;591:11–21.

[20] Otto F, et al. Relative effects of enthalpy and entropy on the phase stability of equiatomic high-entropy alloys. Acta Mater 2013;61(7):2628–38.

[21] Otto F, et al. Decomposition of the single-phase high-entropy alloy CrMnFeCoNi after prolonged anneals at intermediate temperatures. Acta Mater 2016;112:40–52.

[22] Pickering EJ, et al. Precipitation in the equiatomic high-entropy alloy CrMnFeCoNi. Scripta Mater 2016;113:106–9.

[23] Sun SJ, et al. Enhanced strength and ductility of bulk CoCrFeMnNi high entropy alloy having fully recrystallized ultrafine-grained structure. Mater Des 2017;133:122–7.

[24] Gludovatz B, et al. A fracture-resistant high-entropy alloy for cryogenic applications. Science 2014;345(6201):1153–8.

[25] Schuh B, et al. Mechanical properties, microstructure and thermal stability of a nanocrystalline CoCrFeMnNi high-entropy alloy after severe plastic deformation. Acta Mater 2015;96:258–68.

[26] Zhu ZG, et al. Compositional dependence of phase formation and mechanical properties in three CoCrFeNi-(Mn/Al/Cu) high entropy alloys. Intermetallics 2016;79:1–11.

[27] Thürlová H, Průša F. Influence of the Al content on the properties of mechanically alloyed CoCrFeNiMnXAl20−X high-entropy alloys. Materials 2022;15(22).

[28] Strakosova A, et al. Phase and mechanical properties response of the mechanically alloyed CoCrFeNiAlX high entropy alloys. Manufacturing Technology 2022;22(4):471–6.

[29] Kratochvíl P, Průša F. CoCrFeNiTi high entropy alloy prepared via mechanical alloying and spark plasma sintering. Manufacturing Technology 2022;22(4):423–8.

[30] Wong S-K, et al. Microstructures and properties of Al0.3CoCrFeNiMnx high-entropy alloys. Mater Chem Phys 2018;210:146–51.

[31] Varvenne C, Luque A, Curtin WA. Theory of strengthening in fcc high entropy alloys. Acta Mater 2016;118:164–76.

[32] Zhao L, et al. High throughput synthesis enabled exploration of CoCrFeNi-based high entropy alloys. J Mater Sci Technol 2022;110:269–82.

[33] Chang M-P, et al. Effect of manganese on mechanical properties and deformation mechanism of CoCrFeNi high entropy alloys. Mater Today Commun 2023;35:105844.

[34] Gwalani B, et al. Strengthening of Al0.3CoCrFeMnNi-based ODS high entropy alloys with incremental changes in the concentration of Y2O3. Scripta Mater 2019;162:477–81.

[35] Li J, et al. Additive manufacturing of high-strength CrMnFeCoNi high-entropy alloys-based composites with WC addition. J Mater Sci Technol 2019;35(11):2430–4.

[36] Yim D, et al. Fabrication and mechanical properties of TiC reinforced CoCrFeMnNi high-entropy alloy composite by water atomization and spark plasma sintering. J Alloys Compd 2019;781:389–96.

[37] Průša F, et al. Properties of a high-strength ultrafine-grained CoCrFeNiMn high-entropy alloy prepared by short-term mechanical alloying and spark plasma sintering. Mater Sci Eng, A 2018;734:341–52.

[38] Wu Z, et al. Recovery, recrystallization, grain growth and phase stability of a family of FCC-structured multi-component equiatomic solid solution alloys. Intermetallics 2014;46:131–40.

[39] Wang J, et al. Effects of inter-layer remelting frequency on the microstructure evolution and mechanical properties of equimolar CoCrFeNiMn high entropy alloys during in-situ powder-bed arc additive manufacturing (PBAAM) process. J Mater Sci Technol 2022;113:90–104.

[40] Bai Y, et al. Phase transition and heterogeneous strengthening mechanism in CoCrFeNiMn high-entropy alloy fabricated by laser-engineered net shaping via annealing at intermediate-temperature. J Mater Sci Technol 2021;92:129–37.

[41] Zhang Y, et al. Sintering mechanism and microstructure evolution of a CoCrFeNiMn high entropy alloy fabricated by metal injection molding. J Alloys Compd 2021;868:158711.

[42] Ternero F, et al. Influence of the total porosity on the properties of sintered materials—a review. Metals 2021;11. https://doi.org/10.3390/met11050730.

[43] Shao Y, et al. Fabrication and characterization of NbC-CoCrFeNiMn high-entropy alloy cermets. Int J Refract Metals Hard Mater 2021;94:105388.

[44] Laplanche G, et al. Phase stability and kinetics of σ-phase precipitation in CrMnFeCoNi high-entropy alloys. Acta Mater 2018;161:338–51.

[45] Shahmir H, et al. Microstructure tailoring to enhance mechanical properties in CoCrFeNiMn high-entropy alloy by Ti addition and thermomechanical treatment. Mater Char 2021;182:111513.

[46] Praveen S, Murty BS, Kottada RS. Phase evolution and densification behavior of nanocrystalline multicomponent high entropy alloys during spark plasma sintering. JOM 2013;65(12):1797–804.

[47] Praveen S, Murty BS, Kottada RS. Alloying behavior in multi-component AlCoCrCuFe and NiCoCrCuFe high entropy alloys. Mater Sci Eng, A 2012;534:83–9.

[48] Jiang L, et al. Annealing effects on the microstructure and properties of bulk high-entropy CoCrFeNiTi0.5 alloy casting ingot. Intermetallics 2014;44:37–43.

[49] Christofidou KA, et al. On the prediction and the formation of the sigma phase in CrMnCoFeNix high entropy alloys. J Alloys Compd 2019;770:285–93.

[50] Hosseini VA, et al. Effect of sigma phase morphology on the degradation of properties in a super duplex stainless steel. Materials 2018;11(6):933.

[51] Li Y, et al. The electronic, mechanical properties and theoretical hardness of chromium carbides by first-principles calculations. J Alloys Compd 2011;509(17):5242–9.

[52] Rahimi R, et al. Thermal analysis of the formation and dissolution of Cr-rich carbides in Al-alloyed stainless steels. Adv Eng Mater 2019;21(5):1800658.

[53] Laplanche G. Growth kinetics of σ-phase precipitates and underlying diffusion processes in CrMnFeCoNi high-entropy alloys. Acta Mater 2020;199:193–208.

[54] Ganguly A, Murthy V, Kannoorpatti K. Structural and electronic properties of chromium carbides and Fe-substituted chromium carbides. Mater Res Express 2020;7(5):056508.

[55] Xie Y, et al. Effects of N addition on microstructure and mechanical properties of CoCrFeNiMn high entropy alloy produced by mechanical alloying and vacuum hot pressing sintering. Intermetallics 2018;93:228–34.

[56] Peng YB, et al. Microstructures and mechanical properties of FeCoCrNi-Mo High entropy alloys prepared by spark plasma sintering and vacuum hot-pressed sintering. Mater Today Commun 2020;24:101009.

[57] Rogal Ł, et al. Effect of SiC nano-particles on microstructure and mechanical properties of the CoCrFeMnNi high entropy alloy. J Alloys Compd 2017;708:344–52.

[58] Sathiyamoorthi P, et al. Thermal stability and grain boundary strengthening in ultrafine-grained CoCrFeNi high entropy alloy composite. Mater Des 2017;134:426–33.

[59] Zhang M, et al. High-temperature tribological behavior of CoCrFeNiV high-entropy alloys: a parallel comparison with CoCrFeNiMn high-entropy alloys. Tribol Int 2022;174:107736.

[60] Mehranpour MS, Shahmir H, Nili-ahmadabadi M. Microstructure and excess free volume of severely cold shape rolled CoCrFeNiMn high entropy alloy. J Alloys Compd 2020;840:155672.

[61] Wang P, et al. Additively manufactured CoCrFeNiMn high-entropy alloy via pre-alloyed powder. Mater Des 2019;168:107576.

[62] Mehranpour MS, Shahmir H, Nili-ahmadabadi M. Precipitation kinetics in heavily deformed CoCrFeNiMn high entropy alloy. Mater Lett 2021;288:129359.

[63] Oliver WC, Pharr GM. Measurement of hardness and elastic modulus by instrumented indentation: advances in understanding and refinements to methodology. J Mater Res 2004;19(1):3.

[64] Nix WD, Gao H. Indentation size effects in crystalline materials: a law for strain gradient plasticity. J Mech Phys Solid 1998;46(3):411–25.

[65] Haglund A, et al. Polycrystalline elastic moduli of a high-entropy alloy at cryogenic temperatures. Intermetallics 2015;58:62–4.

[66] Hadraba H, et al. Oxide dispersion strengthened CoCrFeNiMn high-entropy alloy. Mater Sci Eng, A 2017;689:252–6.

[67] Laplanche G, et al. Temperature dependencies of the elastic moduli and thermal expansion coefficient of an equiatomic, single-phase CoCrFeMnNi high-entropy alloy. J Alloys Compd 2015;623:348–53.

[68] Rogal Ł, Kalita D, Litynska-Dobrzynska L. CoCrFeMnNi high entropy alloy matrix nanocomposite with addition of Al2O3. Intermetallics 2017;86:104–9.

[69] Guo Z, et al. Microstructure, mechanical and tribological properties of CoCrFeNiMn high entropy alloy matrix composites with addition of Cr3C2. Tribol Int 2020;151:106436.

[70] Asghari-Rad P, et al. TiC-reinforced CoCrFeMnNi composite processed by cold-consolidation and subsequent annealing. Mater Lett 2021;303:130503.

[71] Zhang X, et al. Nanostructured oxide-dispersion-strengthened CoCrFeMnNi high-entropy alloys with high thermal stability. Adv Eng Mater 2021;23(9):2100291.

[72] Zhang M, et al. Tribological behavior of CoCrFeNiMn high-entropy alloy against 304, Al2O3 and Si3N4 counterparts. Wear 2022:204471.